Hot-press sintering of aluminum nitride nanoceramics

Aoyan Liang⊙, Chang Liu⊙, and Paulo S. Branicio⊙*
Mork Family Department of Chemical Engineering and Materials Science, University of Southern California,
Los Angeles, California 90089, USA

The increasing interest in nanostructured ceramics and their applications highlights the need to understand the hot-press sintering of nanoscale AlN powders. We use molecular dynamics simulations to investigate the hot-press sintering of AlN nanoceramics and to clarify the underlying sintering mechanisms. We consider samples with 32 nanoparticles with diameters 8, 12, and 16 nm, arranged in a face centered cubic supercell: samples AlN-8, AlN-12, and AlN-16. Sintering simulations are performed at $T = 1900$ K under 1 GPa for 6 ns. An additional simulation is performed for a sample with 8 nm sized nanoparticles at a lower pressure of 0.1 GPa, namely, sample AlN-8-0.1. After 6 ns, densifications of 99%, 96.2%, 95.6%, and 93.2% are achieved for samples AlN-8, AlN-8-0.1, AlN-12, and AlN-16, respectively. Analysis shows that the fast densification process is rooted at the high diffusivity of nanoparticles surface atoms. The AlN-8 sample undergoes intense microstructural evolution during the sintering process from 3 to 6 ns, resulting in a wide distribution of grain sizes from 4 to 15 nm and a larger, 11 nm average grain size. A slower grain growth process is observed in the AlN-8-0.1 sample from ~4.0 ns. These results indicate a change in the densification mechanism from surface diffusion to grain boundary migration and relaxation of grain boundaries and triple junctions, resulting in a two-stage sintering process, i.e., initially the sample experiences a fast densification, which is followed by intense microstructural evolution. The densification mechanism crossover occurs at 98.7% and 95% densification for the AlN-8 and AlN-8-0.1 samples, respectively. The results indicate that the onset of the second stage depends on a densification threshold, which can be delayed by applying higher external pressure. Sintering of the AlN-16 sample indicates the presence of structural phase transformation at the nanoparticles contact points, which reach over 12 GPa of local pressure during the 1 GPa compression. These results provide atomistic insights into the hot-press sintering of nanoscale ceramics, highlighting the intrinsic swift densification and microstructural evolution processes.

I. INTRODUCTION

Aluminum nitride (AlN) is an important member of advanced technical ceramics. It displays high strength, excellent thermal conductivity, high electrical resistivity, low dielectric constant, and a thermal expansion coefficient compatible with silicon [1–4]. AlN has a wide range of applications in piezoelectric transducers, high power devices, heat exchangers, and optoelectronic and optomechanical devices [5–10]. Due to its strong covalent bonds and thermal stability, the sintering process of AlN is commonly performed at high temperature ~1900 K and high pressure [11,12]. In order to facilitate the sintering process at lower temperatures and low pressure, different sintering aids can be used, such as yttrium oxide (Y_2O_3) [13], cerium oxide (CeO_2) [14], and calcium oxide (CaO) [15]. However, the incorporation of sintering aids may introduce undesired grain boundary phases and impurities that affect sought-after properties of AlN such as its high thermal conductivity [12,16]. An effective way to sinter high purity AlN ceramics without resorting to sintering aids is by using nanoscale AlN powders as starting materials [11,17,18]. Because of the extremely small size and high surface to volume ratio, the driving force for sintering nanoscale powders is

much larger than that of microsized powders [19,20]. Thus AlN nanopowder is expected to display swift sintering densification [21] that was shown by Panchula and Ying [11], who showed nanocrystalline AlN densification of more than 95% at 1700 °C by pressureless and additive-free sintering for 2 hours. The same densification level would require several hours of sintering at 1900 °C for micron-sized powders [11]. Besides promoting the sintering process, the use of nanosized particles in the sintering is reported to enhance the overall mechanical properties of AlN, including hardness, strength, and wear resistance [16,22].

Besides the use of nanoscale powders, the sintering of AlN ceramics can also be enhanced with simultaneous application of heat and pressure, in what is known as hot-press or hot isostatic press sintering [21,23]. Compared to pressureless-sintering, hot-pressing sintering accelerates the densification process and reduces the sintering temperature [24–26]. The hot-press sintering process and its densification mechanisms for various ceramics have been investigated over the past decades [27–31]. Nguyen *et al.* [30] studied the densification mechanisms of ZrB_2-SiC ceramics using hot-press sintering and found a temperature dependence of the densification mechanisms. At low temperatures, the dominant sintering mechanisms are plastic deformation and particle rearrangement/fragmentation, while at high temperatures the dominant sintering mechanism is diffusion. Hot-press sintering of boron

*Corresponding author: branicio@usc.edu

carbide performed by Du *et al.* [27] indicates a shift of sintering mechanisms from plastic deformation to grain-boundary diffusion during the densification process. Although the densification mechanisms during the hot-press sintering process of micron-sized ceramic powders have been investigated and clarified, the mechanisms of nanoscale AlN powders, especially the nanoparticle behavior under high pressure, are not well understood.

One of the challenges of sintering nanoscale powders by hot-press sintering is the tendency of the microstructure to undergo coarsening during the densification [32]. Thus, besides clarifying the densification mechanisms, it is important to investigate the microstructural evolution and the grain growth process during the sintering. According to Fang *et al.* [33], the grain growth during the sintering of nanoparticles can be divided into two steps: grain coarsening and rapid grain growth. Grain coarsening refers to the initial slow grain growth during the early stages of sintering, while the rapid grain growth occurs when the densification reaches a critical value where grain boundaries become mobile. Many studies have reported the presence of rapid grain growth during the sintering processes of nanoparticles [34–38]. For hot-press sintering of micron-sized powders, the grain growth mechanisms and the effects of pressure and temperature on the grain growth are reasonably understood [34,35,39]. Nonetheless, the grain size evolution dynamics during the hot-press sintering of nanoceramics and the critical densification value that triggers the rapid grain growth are not clear.

Molecular dynamics (MD) simulations are well suited for investigating the hot-press sintering mechanisms and the microstructural evolution of nanoscale powders [40]. The sintering process of many different nanoparticles have been successfully investigated by MD in the past, including sintering of silicon [41], nickel [42], silicon carbide [43,44], and titanium dioxide [45–47]. However, most of these studies were focused on the modelling of few, typically two or three, nanoparticles. Therefore, while meaningful insights were obtained from these previous simulations, they do not offer a full description of the hot-press sintering mechanisms and related microstructural evolution of a strong technical ceramic material such as AlN.

In this work, we investigate the densification process and microstructural evolution during the hot-press sintering process of nanoscale AlN powders by performing large scale MD simulations. The effects of nanoparticle size and external pressure are explored by employing three nanoparticle sizes, 8, 12, and 16 nm, and two hydrostatic pressures, 0.1 and 1 GPa. Results show that higher external pressure accelerates the densification and grain growth processes, and smaller particle size improves the sinterability of AlN ceramics. Densification as high as 99% as well as swift grain growth are achieved within 6 ns for the smallest nanoparticle considered (8 nm) under the high pressure of 1 GPa. These results provide atomistic insights into the hot-press sintering of nanoceramics.

II. METHODS AND SIMULATION PROCEDURES

We consider three samples with dimensions about $22.5 \times 22.5 \times 22.5$, $33.4 \times 33.4 \times 33.4$, and $44.7 \times 44.7 \times 44.7$ nm^3, containing 815 040, 2 749 248, and
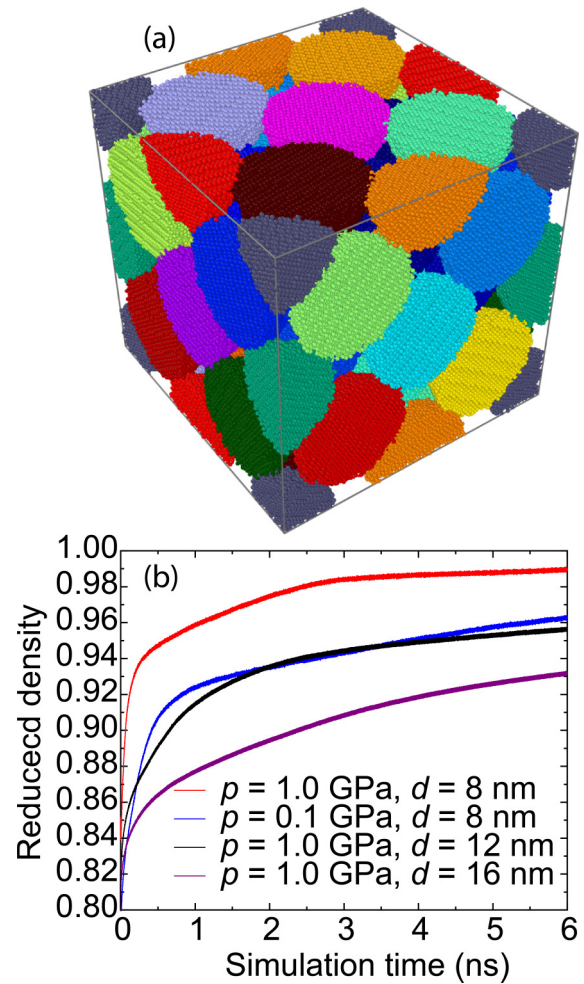

FIG. 1. Illustration of the hot-press sintering of AlN simulated by molecular dynamics. (a) Illustration of the simulation model composed of 32 nanoparticles of 8 nm diameter, arranged in a face centered cubic supercell. Different colors indicate different nanoparticles. (b) Densification during the sintering process for different pressures and particle sizes.

6 517 568 atoms, respectively. Each sample consists of 32 AlN nanoparticles arranged in a face centered cubic (FCC) supercell, as shown in Fig. 1(a). Each spherically shaped nanoparticle is a defect free wurtzite single crystal with a random orientation. The diameters of the nanoparticles in the three samples are 8, 12, and 16 nm, respectively. All three samples are sintered at 1900 K under a hydrostatic pressure of 1 GPa for 6 ns. We will refer to them as samples AlN-8, AlN-12, and AlN-16. As a comparison, another sample with 8 nm sized nanoparticles is sintered at a lower hydrostatic pressure of 0.1 GPa, which will be referred to as sample AlN-8-0.1. The hot-press sintering MD simulations are implemented using the following schedule:

(1) set the external pressure to 0.1 or 1.0 GPa and relax for 15 ps at 300 K;

(2) increase the temperature to 900 K and thermalize for 15 ps;

(3) increase the temperature to 1,400 K and thermalize for 15 ps;

(4) increase the temperature to 1,900 K and sinter for 6 ns.

All the steps are performed in the NPT ensemble with periodic boundary conditions along all three directions. A time step of 1.5 fs is used in the integration of the equations of motion following previous investigations of AlN [48]. The forces between Al and N atoms are derived from two-body and three-body interactions, which can be expressed as

$$V = \sum_{i<j} V_{ij}^{(2)}(r_{ij}) + \sum_{i,j<k} V_{jik}^{(3)}(r_{ij}, \, r_{ik}), \qquad (1)$$

where the two-body term $V_{ij}^{(2)}(r_{ij})$ consists of van der Waals interactions, Coulomb interactions, steric-size effects, and charge-induced dipole:

$$V_{ij}^{(2)}(r_{ij}) = -\frac{W_{ij}}{r_{ij}^6} + \frac{Z_i Z_j}{r_{ij}} e^{-\frac{r_{ij}}{\lambda}} + \frac{H_{ij}}{r_{ij}^{\eta_{ij}}} - \frac{D_{ij}}{r_{ij}^4} e^{-\frac{r_{ij}}{\xi}}, \qquad (2)$$

In Eq. (2), r_{ij} is the distance between the ith atom and the jth atom, W_{ij} and D_{ij} are the strength of the van der Waals attraction, Z_i is the effective charge in units of electric charge e, λ and ξ are the screening lengths for the Coulomb and charge-dipole interactions, and H_{ij} and η_{ij} are the strength and exponent of the steric repulsion. The three-body term $V_{jik}^{(3)}(r_{ij}, \, r_{ik})$, representing covalent interactions, can be written as a product of spatial and angular dependent factors that reflect bond-bending and bond-stretching characteristics:

$$V_{jik}^{(3)}(r_{ij}, \, r_{ik}) = R^{(3)}(r_{ij}, \, r_{ik}) P^{(3)}(\theta_{jik}). \qquad (3)$$

The expressions for the spatial dependent factor $R^{(3)}(r_{ij}, \, r_{ik})$ and the angular dependent factor $P^{(3)}(\theta_{jik})$ are given by Eqs. (4) and (5):

$$R^{(3)}(r_{ij}, \, r_{ik}) = B_{jik} \exp\left(\frac{\gamma}{r_{ij} - r_0} + \frac{\gamma}{r_{ik} - r_0}\right)$$
$$\Theta(r_0 - r_{ij})\Theta(r_0 - r_{ik}), \qquad (4)$$

$$P^{(3)}(\theta_{jik}) = \frac{(\cos\theta_{jik} - \cos\bar\theta_{jik})^2}{1 + C_{jik}(\cos\theta_{jik} - \cos\bar\theta_{jik})^2}. \qquad (5)$$

where B_{jik} represents the strength of the three-body interaction, $\Theta(r_0 - r_{ij})$ is the step function, θ_{jik} is the angle formed by $\vec{r}_{ij}$ and $\vec{r}_{ik}$, $\bar\theta_{jik}$ and C_{jik} are constants. Values for all the parameters are provided in Vashishta *et al.* [49]. Parameters are fitted and validated by experimental results on lattice constants, elastic moduli, cohesive energy, melting temperature, and the pressure-induced wurtzite-to-rocksalt structural phase transformation [49]. A comparison between three interatomic potentials for AlN shows that Vashishta many-body potential can provide accurate predictions and is suitable for many applications [50]. This interatomic potential for AlN has been successfully applied in several previous studies of plane shock loading, nanoindentation, projectile impact, and the mechanical behavior of the AlN amorphous phase [48,51–55]. The same potential form has also been successfully applied in the investigations of other similar ceramics, such as SiC [56–61] and Al_2O_3 [62,63].

III. RESULTS

As a first step in the investigation of the hot-press sintering of AlN nanopowders, we focus on the densification profiles as a function of time and the influences of initial particle size and pressure. From the hot-press sintering, at 1,900 K and 1 GPa pressure, of the AlN-8, AlN-12, and AlN-16 samples, we calculate the evolution of the reduced density (ρ/ρ_0), which is shown in Fig. 1(b). One additional curve shows the result for the sample AlN-8-0.1, which is sintered at 0.1 GPa pressure. The densifications of all four samples follow a two-step regime, with a sharp increase in the first few picoseconds followed by a much lower densification rate. The initial reduced density is set mathematically by the atomic packing factor of the FCC arrangement of the AlN nanoparticles, 74%. This reduced density increases swiftly in all cases to beyond 86% at 0.5 ns of sintering. The results show a strong effect of the particle size on the observed densification rate, with larger nanoparticles displaying noticeable lower densification rates. Moreover, a comparison of the densification profiles of samples AlN-8 and AlN-8-0.1 indicates that the application of high pressure is an effective way to enhance the densification rate and promote consolidation of AlN nanopowders. One can note that there is a clear densification rate decline for all systems as a function of sintering time, in particular for the AlN-8. At ∼3.0 ns, the densification curve of the AlN-8 sample nearly halts, increasing from 98.7% to 99% in the next 3 ns of sintering. Nevertheless, the AlN-8 experiences significant microstructural evolution during the last 3 ns of sintering as will be discussed. After hot-press sintering for 6 ns, the highest densification at 99% is achieved by the AlN-8 sample followed by AlN-8-0.1, AlN-12, and AlN-16 at densifications of 96.2%, 95.6%, and 93.2%, respectively.

After 6 ns of hot-press sintering, the different samples simulated present contrasting porosities and microstructures. Illustrations of the microstructures and their remaining pore structures are presented in Fig. 2. In Figs. 2(a)–2(d), the grains in each sample are shown by different colors. Grains are identified by using a combination of different methods such as polyhedral template matching, graph clustering, and others, as implemented in OVITO [64–66]. As shown in Fig. 2(a), the shape and size of each grain in sample AlN-8 change significantly compared with the initial spherical shape of the nanoparticles, as shown in Fig. 1(a). Some of the grains in the final AlN-8 sample become particularly large at the expense of others that shrink and eventually disappear, suggesting the occurrence of a swift grain growth process. In contrast, such grain growth process is not apparent in samples AlN-8-0.1, AlN-12, and AlN-16 after sintering for 6 ns. Thus we can infer that the combination of small particle size and high pressure can lead to a swift grain growth process during the hot-press sintering of AlN nanopowders. Furthermore, the sample AlN-8-0.1 forms much larger relative necking areas between nanoparticles than samples AlN-12 and AlN-16, i.e., a larger area of contact between two grains scaled by the particle size. That further indicates that the sintering process of small nanoparticles is faster than large nanoparticles. In order to analyze the residual porosity in each sample after the sintering process, we use a surface reconstruction method that is set to identify pores that can minimally fit a spherical
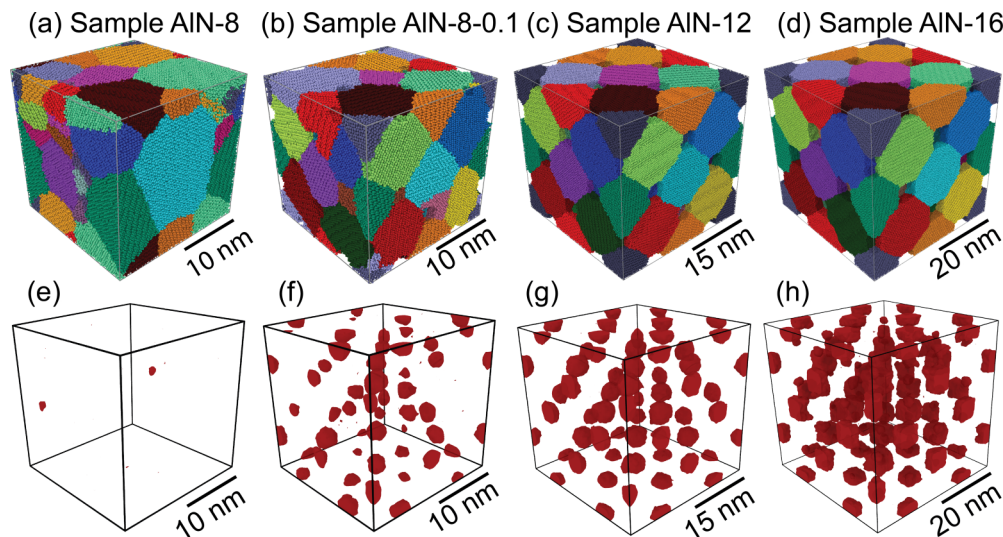
FIG. 2. Illustration of the of AlN supercells and their corresponding pores after hot-press sintering for 6 ns. [(a) and (e)] $p = 1.0$ GPa, $d = 8$ nm. [(b) and (f)] $p = 0.1$ GPa, $d = 8$ nm. [(c)and (g)] $p = 1.0$ GPa, $d = 12$ nm. [(d) and (h)] $p = 1.0$ GPa, $d = 16$ nm. Different colors indicate different grains.

volume with radius of ∼2.8 Å [64,67]. The contrasting results are illustrated in Figs. 2(e)–2(h). As a result of neck growth and microstructural evolution, pores are nearly eliminated in the sample AlN-8. Nonetheless, the other three samples still display pores at most, or all the initial cavities defined by the FCC supercell interstitial locations. The results show a direct inverse relationship between densification and the volume of the residual pores (see Ref. [68] at Fig. S1 for porosity evolution during the sintering process). As a consequence, after the AlN-8 sample, the sample AlN-8-0.1 displays the smallest pore sizes. Several pores in the sample AlN-8-0.1 have in fact disappeared during the 6 ns hot-press sintering, while all pores are still present in samples AlN-12 and AlN-16, albeit with diminished volumes.

To further understand the fast densification process of AlN nanopowders during the hot-press sintering, we calculate the mean square displacement (MSD) of Al and N atoms in samples AlN-8 and AlN-8-0.1. In the calculation of the MSD, we divide each nanoparticle in the initial system into three regions in order to quantify the MSD of atoms close to surface (first shell), close to the core (Core), and in between (second shell). The thickness of the shells is defined to be 1 nm while the core region has a radius of 2 nm, as shown in Fig. 3(a). During the hot-press sintering the MSD for the atoms in these initial regions is calculated and monitored separately. The MSD for Al and N atoms in the different regions are shown in Figs. 3(b) and 3(d). The results clearly show that the MSD in the first shell is about an order of magnitude larger than the MSD in the core region during the sintering. While the MSD for the second shell is noticeably larger than that of the core region, it is several times smaller than that of the first shell, during the whole sintering process. The diffusion coefficient, D, can be directly calculated from the slope of the MSD curves at very long simulation times by $D = \lim_{t \to \infty} \text{MSD}(t)/6t$. The D for Al and N atoms in different regions are shown in Figs. 3(c) and 3(e), respectively. As shown in Figs. 3(c) and 3(e), surface atoms have a much larger diffusion coefficient than atoms in

inner regions during the densification process. These results suggest that the densification process of AlN nanopowders is dominated by the fast surface diffusion. In addition, by comparing Figs. 3(b) and 3(c) with 3(d) and 3(e), one can notice that the MSD as well as the diffusion coefficient of Al atoms are about an order of magnitude larger than those of
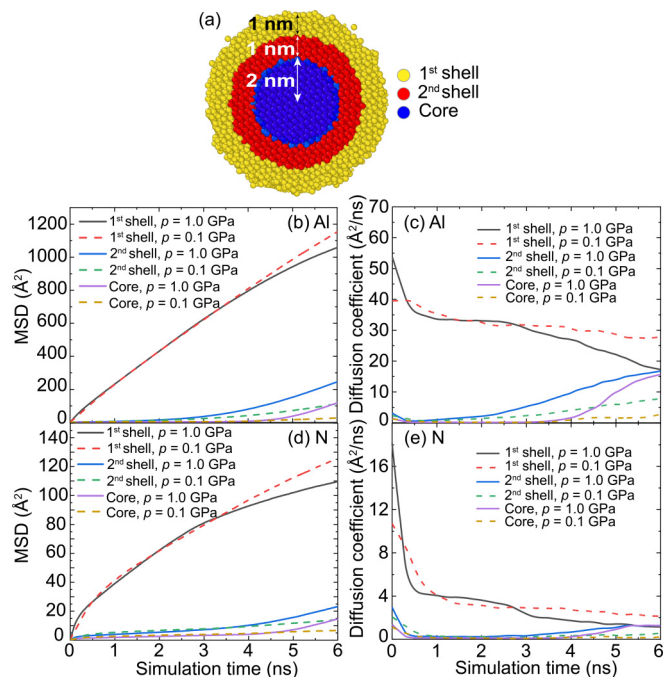

FIG. 3. Mean square displacement (MSD) and diffusion coefficient of aluminum and nitrogen atoms during the sintering of the 8 nm nanoparticle system under different pressures. (a) Cross-section view of the three nanoparticle regions used in the calculations. (b) MSD and (c) diffusion coefficient of Al atoms initially in the different regions shown in (a) for different pressures, and corresponding (d) MSD and (e) diffusion coefficient for N atoms.

N atoms in the same region, indicating that cations drive the surface diffusion process.

It is instructive to analyze the changes in diffusion coefficient curves during the sintering process. The diffusion coefficient for atoms in all three regions drops rapidly in the first 0.3 ns as MSD increases fast due to the sudden change of temperature. After the ballistic region, as densification processes, the diffusion coefficient in the first shell steadily decreases while that in the inner regions slightly increases. However, one can note that the diffusion coefficient in the second shell and core region in the AlN-8 sample increases faster after ∼3.0 and ∼4.0 ns, while that of the first shell decreases faster, see Figs. 3(c) and 3(e). This distinct increasing and decreasing of the diffusion coefficient at different times can be explained by the microstructural evolution, including surface area reduction and grain boundary migration experienced by the AlN-8 sample. At about 3.0 ns, the densification of the sample AlN-8 reaches more than 98%, and most of the pores are eliminated. A fraction of the atoms initially located at the first shell cannot diffuse freely anymore since they have become "bulk" atoms and adopt an associated lower diffusion rate. As a result, the diffusion coefficient of the first shell atoms drops. A fraction of the atoms initially located in the second shell and core region eventually diffuses when they interact or become part of grain boundary regions due to grain boundary migration. As a result, their diffusion coefficients increase when microstructural evolution is triggered. Although the diffusion coefficient for atoms initially in inner regions increases, the average diffusion coefficient of all three layers still decreases, because the first shell contains the largest fraction of the atoms in the system at ∼60% in comparison with the second shell (∼30%) and core region (∼10%). This phenomenon elucidates the low densification rate after ∼3.0 ns for the sample AlN-8. After sintering for 6 ns, the diffusion coefficients in three regions in the sample AlN-8 have almost the same value, indicating that the initial division of atoms does not exist anymore due to the significant microstructural evolution. Besides, as shown in Figs. 3(b) and 3(d), the MSD curves of different regions in samples AlN-8 and AlN-8-0.1 are overlapped before significant microstructural evolution occurs in sample AlN-8. That implies that pressure does not affect the diffusion of Al and N atoms during the early sintering stage.

The changes in the MSD curves of the sample AlN-8 can be further understood by considering the bond angle distribution analysis for the first shell and core regions. Bond angles formed by the atomic triplets: Al-N-Al, Al-N-N, N-Al-N, and Al-Al-N in the first shell and core regions are evaluated before (0 ns) and after (6 ns) sintering and their distributions are shown in Fig. 4. Before sintering, the core region displays (i) well-defined Al-N-Al and N-Al-N bond angle distributions peaked at ∼109.5° and (ii) no wrong bonds, i.e., no Al-N-N or Al-Al-N triplets, showing that the core region is defect free in the beginning. Nonetheless for the first shell, besides the well-defined Al-N-Al and N-Al-N peaks, three additional small amplitude peaks appear: Al-N-Al at ∼80°, Al-Al-N at ∼50° and 120°. As shown in Fig. 5, these discrepancies are related to defects and wrong bonds located in the first shell at both surface and grain boundaries before sintering, while no defects are found in the second shell and core regions.
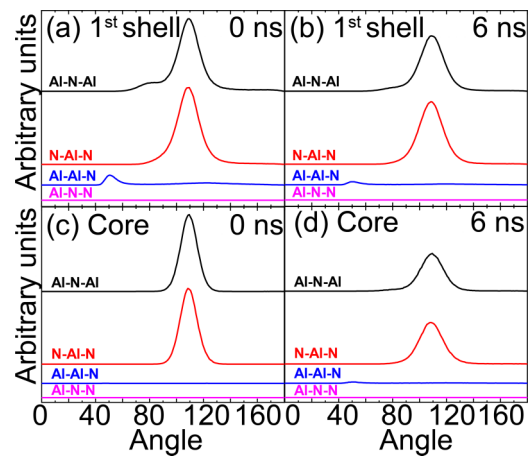

FIG. 4. Bond angle distributions of different layers in the 8 nm nanoparticle system under 1 GPa before and after sintering. (a) First shell before sintering, (b) first shell after sintering, (c) core region before sintering, and (d) core region after sintering.

After sintering for 6 ns, the Al-N-Al and N-Al-N bond angles in both the first shell and core regions still display peaks at ∼109.5°, yet with rather wider distributions, as shown in Fig. 4(b) and 4(d). The intensity of the additional peaks for the first shell decrease, indicating a reduction in the number of wrong bonds and relaxation of the interfacial structure. In contrast, one additional small bond angle peak is generated in the core region at ∼50°, indicating that defects have been generated in the original core regions during the sintering. That is related to grain boundary migration into inner regions of the original nanoparticles, as indicated previously. This grain boundary migration is accompanied by a swift grain growth process as will be discussed.

In order to characterize the grain growth process in the sample AlN-8, we evaluated the grain size distribution at six different time points during the hot-press sintering. As a comparison, the same analysis is also performed on the sample AlN-8-0.1. Here we use the same grain identification method
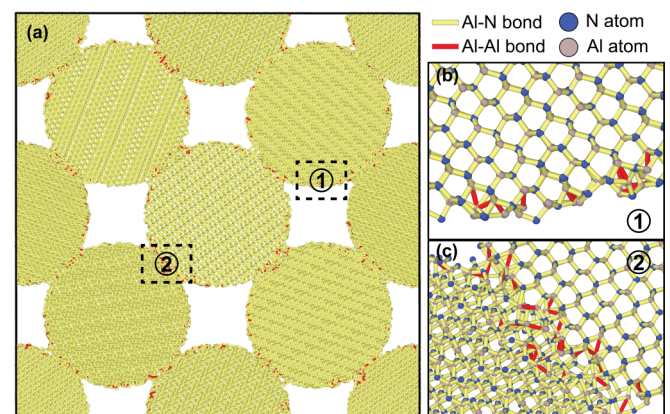

FIG. 5. Cross-section view of the AlN-8 sample before sintering, showing Al-Al and Al-N bonds by yellow and red sticks, respectively. Regions 1 and 2 in (a) highlight the bonding structure at the nanoparticle surface and contacting region, respectively. (b) and (c) shows a zoomed view of regions 1 and 2 indicated in (a).
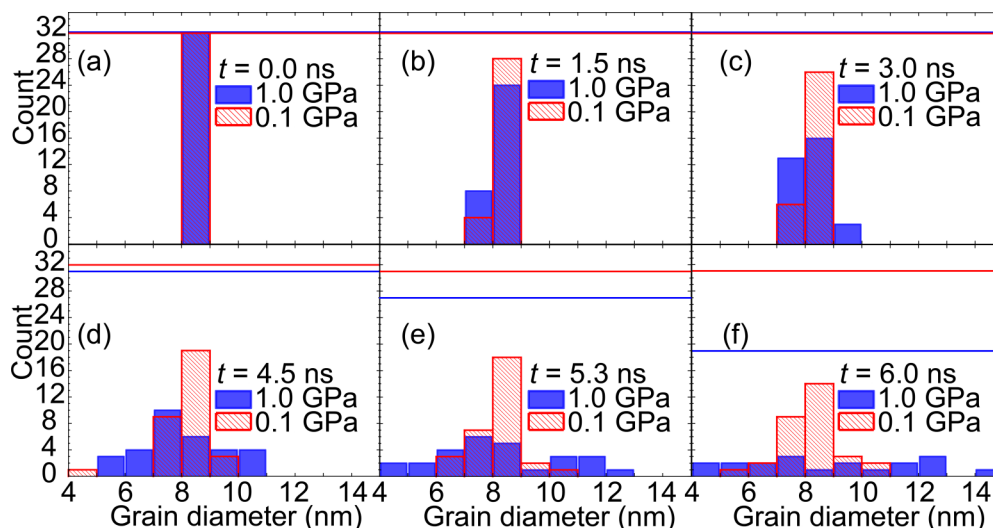
FIG. 6. Evolutions of the grain size distribution for the 8 nm nanoparticle systems during sintering at 1.0 and 0.1 GPa. Blue and red solid lines indicate the total number of grains at 1.0 and 0.1 GPa, respectively. (a) $t = 0.0$, (b) 1.5, (c) 3.0, (d) 4.5, (e) 5.3, and (f) 6.0 ns.

as discussed previously. After a grain is identified its size is calculated by converting the number of atoms to the diameter of a spherical shape, based on the atomic volume of AlN at the sintering temperature, 1900 K. The results are shown in Fig. 6. In the first 3 ns of sintering, the size distribution peaks at 8–9 nm. The results indicate that the distributions gradually become wider for both AlN-8 and AlN-8-0.1 samples with sintering time. However, in the last 3 ns of sintering, the grain size distribution of the sample AlN-8 spreads rapidly, resulting in a wide distribution from 4 to 15 nm with no well-defined peak, suggesting the occurrence of a swift microstructural evolution. During the same time period, the total number of grains in the sample AlN-8 drops from 32 to 19, as small grains shrink and are eliminated, consistent with a grain growth process. In contrast, the evolution of the grain size distribution in the sample AlN-8-0.1 occurs at a much slower pace. The grain size distribution still peaks at 8–9 nm and maintains a lognormal shape from 3 to 6 ns. At 6 ns, the microstructure has lost only one grain and the distribution of grain size lies in the range of 5 to 11 nm. More details about the grain size evolutions for sample AlN-8 and AlN-8-0.1 are provided in Figs. 7(a) and 7(b).

In order to gain further insights into the microstructural evolution and changes in grain size distributions, we evaluate size changes for each of the original 32 grains of the system during sintering. To monitor the size evolution, we must identify and track the grains during the sintering process. The grain tracking algorithm used here considers the center of mass of each grain in all configurations taken at every 7.5 ps. Each grain receives a unique grain id that is produced by identifying the corresponding grain in each subsequent configuration in time by finding the grain with the closest center of mass. New grain generation is not considered in this algorithm, since new grains have subcritical sizes and are unstable, disappearing after a short time. The results are shown in Figs. 7(a) and 7(b), together with the average and weighted average grain sizes, the latter calculated using the number of atoms of each grain as weight. For the grain size evolutions in the AlN-8 sample,

shown in Fig. 7(a), we can see a steady grain growth/shrink rate in the first 3 ns. The rate then intensifies as grain boundary migration is triggered and small grains are eliminated from 3 to 6 ns. The weighted average grain size correspondingly displays a sharp increase after 3 ns and reaches a value exceeding 11 nm at the end of the sintering simulation, indicating a significant microstructural coarsening from 3 to 6 ns. In contrast, except for one grain that shrinks and is eliminated swiftly after 3 ns, the other grains in the AlN-8-0.1 sample keep a nearly constant grain growth/shrink rate resulting in a slightly larger weighted average grain size ($\sim$8.6 nm) at the end of the sintering simulation. That indicates that the microstructural evolution in the AlN-8-0.1 sample is rather sluggish compared to that experienced by the AlN-8 sample.

These results reveal a two-stage microstructural evolution process during the hot-press sintering of AlN nanopowders. The first stage, i.e., first 3 ns of sintering for the AlN-8 sample, is marked by a widening of the grain size distribution, occurring simultaneously with the swift densification process, driven by fast surface diffusion. The second stage, i.e., the last 3 ns of sintering for the AlN-8 sample, is marked by a swift coarsening of the microstructure, when large grains grow swiftly at the expense of small grains, sharply increasing the average grain size. In this last stage samples reach nearly full densification as a result of grain boundary migration and relaxation of interfaces and triple junctions. The results show that the crossover between the two stages of the microstructural evolution can be identified by a critical densification value. To better identify the critical densification value, we plot the weighted average grain size as a function of reduced density for both sample AlN-8 and AlN-8-0.1 in Fig. 7(c). As shown in Fig. 7(c), the grain size keeps a constant value at low densification and then starts increasing swiftly after reaching a certain reduced density. For the AlN-8-0.1 sample, the results indicate that this threshold densification value is $\sim$95%, while this value reaches $\sim$98.7% for the AlN-8 sample, suggesting that this critical densification value depends directly on the sintering pressure. Therefore, we can infer that the use of
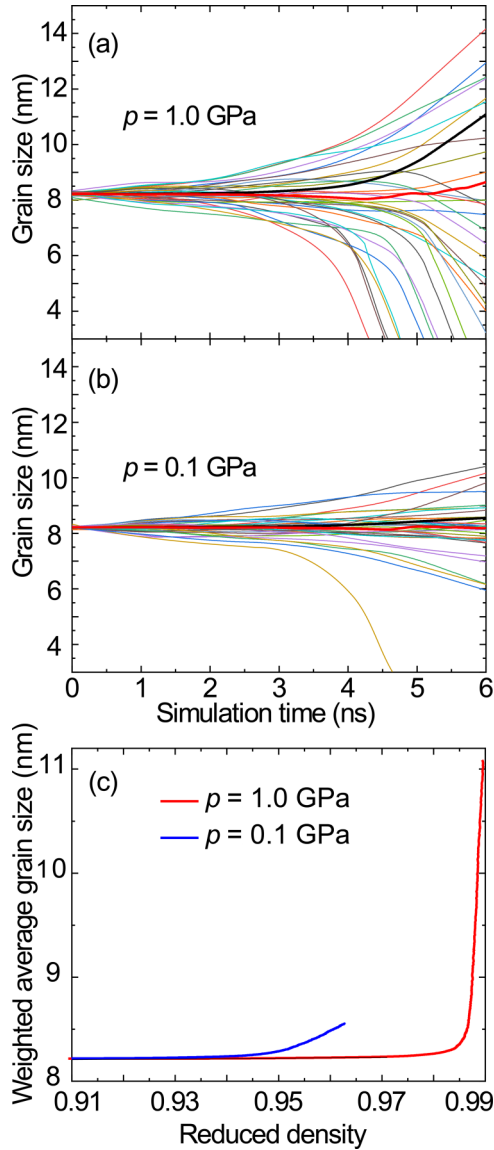
FIG. 7. Grain size evolutions for the 8 nm nanoparticle systems sintered under (a) 1.0 and (b) 0.1 GPa. Each colored line represents one of the initial 32 grains, the black thick line represents the weighted average grain size, and the red thick line represents the average grain size in (a) and (b). The relationship between reduced density and weighted average grain size is shown in (c).

small particle sizes and high pressure is able to accelerate the sintering process as well as delay the onset of rapid grain growth, which makes it possible to produce a fully densified sample without significantly coarsening the microstructure of nanocrystalline ceramics.

IV. DISCUSSIONS

The results obtained in this work provide direct insights on the elusive effect of particle size on the sintering process of ceramics, in particular nanoceramics. Animation movies based on the MD simulations are provided in Ref. [68] to illustrate the sintering process (see Ref. [68], movies 1–5 for the animation movies). The results shown in Fig. 1(b) and Fig. 2 indicate

that the use of small nanoparticles as starting materials leads to a swift sintering densification process, that is able to produce almost fully densified samples without any sintering aids within 6 ns. Several experimental studies have reported the effects of the initial particle size on the densification process of AlN and other ceramics, i.e., the densification rate is enhanced as particle sizes are reduced [11,13,18,69–71]. Based on the nonlinear diffusion law proposed by Pan [19], the sintering rate is several orders of magnitude higher than that predicted by the Coble sintering model [72], when particle sizes are reduced to less than 60 nm. Our results provide further support to experimental reports on microcrystalline AlN and other ceramics and to the work of Pan [19], by demonstrating the enhancement of the densification process with the reduction of particle sizes in the nanoscale. As shown in Fig. 1, all samples display extremely fast sintering rates, among which the sample with the smallest particle size has the highest densification rate.

To further understand the relationship between the densification rate and the sintering conditions, we propose a sintering model based on the reduced density dependence on pressure, grain size, diffusion coefficient, and sintering time. The model is inspired by the late-stage sintering model proposed by Sakai and Iwata [73] as shown in Eq. (6), which was derived from the Nabarro and Herring diffusional creep model [74,75]:

$$-\ln(1-\rho) = \frac{9}{2}\frac{40D\Omega}{kTd^2}(p_2 - p_1)t - \ln(1-\rho_0), \quad (6)$$

where ρ and ρ_0 are the current and initial densities, D is the diffusion coefficient, Ω is the atomic volume, k is the Boltzmann constant, T is the sintering temperature, d is the average grain size, $p_2 - p_1$ is the difference between external pressure and the gas pressure in the pores, and t is the sintering time. By replacing all the parameters in Eq. (6) with the corresponding values in our results, we find that the densification process of nanoparticles shows a much higher densification rate than Sakai and Iwata's late-stage model [73]. In order to better describe and predict the densification process driven by the fast surface diffusion of nanoparticles, we relax the power of each parameter in Eq. (6) and divide the swift densification process into an early and a late stage. The early stage is defined as the initial densification process when the reduced density is less than 94% for samples sintered under 1 GPa and less than 92% for the sample sintered under 0.1 GPa. The late-stage densification proceeds when the reduced density is higher than these reduced density threshold values. The early stage and late-stage densification models for AlN nanoparticles sintered at 1900 K are shown in Eqs. (7) and (8), respectively.

$$-\ln(1-\rho) = 0.043\frac{Dp^{0.25}}{d}t^{0.5} - \ln(1-\rho_0), \quad (7)$$

$$-\ln(1-\rho) = 0.021\frac{Dp^{0.5}}{d^3}t - \ln(1-\rho_1), \quad (8)$$

where ρ and ρ_0 are the current and initial reduced densities, ρ_1 is the threshold reduced density value, either 0.94 or 0.92, D is the average diffusion coefficient during the whole sintering process (AlN-8 and AlN-8-0.1: 11.0 Å^2/ns; AlN-12:
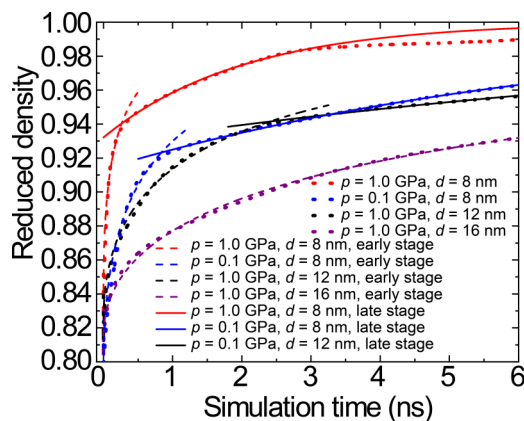
FIG. 8. Densification during the sintering process for different pressures and particle sizes. Models for early stage densification are shown by dashed lines while models for late-stage densification are shown by continuous lines.

6.5 $Å^2$/ns; AlN-16: 5.2 $Å^2$/ns), p is the hydrostatic pressure (GPa), d is the grain size (nm), and t is the sintering time (ps). Equation (7) indicates a linear relationship between $-\ln(1-\rho)$ and $t^{0.5}$ in the early stage, while Eq. (8) shows a linear relationship between $-\ln(1-\rho)$ and t in the late stage. This linear relationship in the late-stage model corresponds to the sintering model in Eq. (6). Nonetheless, our model displays different dependencies of pressure and grain size on the densification, i.e., the densification of AlN nanoparticles has higher dependence of grain size yet lower dependence of pressure. The densification rates in both early and late stages are proportional to the pressure and inversely proportional to the grain size, suggesting that high pressure and small grain size accelerate the densification process. That is particularly the case for the late-stage densification, which shows higher powers of pressure and grain size than the early stage model. Both early and late-stage models are plotted in Fig. 8, which displays excellent fittings for all samples. The crossover between early and late-stage densifications is clearly indicated by the crossing of the fitting curves. One should note that there is a discrepancy between the densification data and the late-stage model for the AlN-8 sample, starting at ~3 ns. The densification process nearly halts when the AlN-8 sample reaches ~98.7% densification because of the significant microstructural evolution that occurs from ~3 ns to 6 ns. One startling prediction of this analysis is that the AlN-16 sample is still in the early stage densification process at 6 ns. That suggests that samples with small grain size are more likely to experience swift grain growth due to the large densification rate. These two models provide an excellent description of the densification process and can be used to predict the hot-press sintering process of AlN nanoceramics. More data would be required to include the sintering temperature as a variable into the models.

Even though the reduction of grain sizes enhances the densification rate in the sintering of ceramics, it has been reported that it may also adversely affect the sintering process aided by additives [76,77]. For example, Li *et al.* [76] investigated the effect of particle size on the sintering process of silicon carbide, using magnesium alloy powders as additives.

They reported that the sintered sample with smaller particles (90 nm) displayed extremely low densification (48.45%) due to the large size difference between silicon carbide and additive particles (86 μm). The small silicon carbide particles tended to agglomerate preventing an effective interaction with the large additive particles. Zou *et al.* [77] also reported that the densification of BaTiO$_3$ ceramics were lower if the particle size of BaTiO$_3$ was not distinctly larger than that of glass sintering aids. That suggests that to enhance the densification when sintering aids are used, one must carefully consider the particle sizes of sintering materials and additives.

Our results show that high external pressure significantly enhances the densification process of AlN, in agreement with several experimental investigations of the sintering process of different ceramics [25,26,78–83]. For example, Barick *et al.* [78] investigated the effect of pressure on the densification of silicon carbide during spark plasma sintering. Their results showed that the relative density of the sintered sample could be increased from 77% to 95.5% with an increase in pressure from 22 to 75 MPa at the same sintering temperature. In this work, as shown in Fig. 1(b), the densification of the AlN sample with 8 nm sized particles increases from 96.2% to 99%, when hydrostatic pressure is increased from 0.1 to 1.0 GPa. According to the MSD results shown in Figs. 3(b) and 3(c), there are no clear differences between the MSD evolutions of the AlN-8 and AlN-8-0.1 samples in the first 3 ns of sintering, indicating that high external pressure does not affect the Al and N diffusivities. This result contrasts with a theoretical sintering model proposed by Liao *et al.* [26], in which high pressure was expected to limit the diffusion of atoms, arguably due to the reduction in the vacancy volume with application of high pressure. One reason for the contrast in theoretical and simulation predictions is that there are no vacancies in the initial nanoparticles in the simulations here. All vacancies are introduced during the sintering process when the nanoparticles (grains) absorb vacancies from the pore regions. An accurate method to localize point defects such as interstitials and vacancies is the Wigner-Seitz cell method [84], which requires a defect-free crystal structure as a reference. However, it is challenging to utilize such method in our simulations because of the strong dynamic evolution of the samples and the high temperature. Although it is nontrivial to visualize the vacancies directly, we can show the presence of interstitials by analyzing the abnormal bonds formed, which indirectly indicate the existence of vacancies. Here, we select the sample AlN-16 at 6 ns as a general case for samples experiencing the early stage densification. A slab with a thickness of 2 nm is used for analysis and the results are shown in Fig. 9. As shown in Fig. 9(a), a large necking area has formed between particles, where some small rocksalt grains form, as will be discussed later. The abnormal Al-Al bonds in the selected slab are shown in Fig. 9(b). In addition to the defects and wrong bonds located on the surface and in grain boundaries, as shown in Fig. 5, the results indicate the presence of Al-Al wrong bonds inside the grains. Such wrong bonds are formed between an interstitial Al atom with other Al atoms of the wurtzite structure, suggesting that interstitials and vacancies are generated and further propagate into the inner regions during the early sintering stage while the pore volume decreases. The early stage MSD for different regions shown in
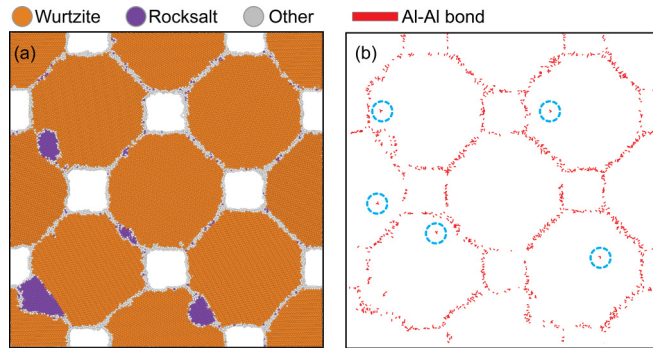
FIG. 9. Cross-section view of the AlN-16 sample after sintering for 6 ns. (a) Cross-section view of the crystalline structure with atoms colored by the phases they form. (b) Spatial distribution of Al-Al bonds for the cross-section shown in (a). The blue dashed circles in (b) highlight the location of Al-Al wrong bonds inside the grains. Such in-grain wrong bonds are indicative of the presence of interstitial-vacancy pairs.

Figs. 3(b) and 3(d) are dominated by surface atomic diffusion. Therefore the diffusivity is not affected by pressure in the first 3 ns of sintering. The fast densification rate under high pressure in the early sintering stage is mainly due to the fast pore volume shrink rate driven by the fast surface diffusion. After 3 ns, when densification reach high levels, as pores are nearly eliminated, the diffusivity of the first shell atoms in AlN-8 and AlN-8-0.1 samples start to diverge as the number of surface atoms in the AlN-8 sample is severely reduced with the shrinkage of the pores. In the second stage, from 3 ns to 6 ns of sintering, MSD is enhanced in the second shell and core regions as grain boundaries migrate into these regions. In the case of the AlN-8 sample, grain boundary migration also enhances the MSD in those regions. These results provide further insights into the effects of pressure on the densification of nanoparticles during the sintering process.

After having discussed the effects of small particle size and high pressure on the sintering rate of nanoceramics, it is instructive to revisit the hot-press sintering mechanisms of AlN nanoparticles on the light of reports on sintering mechanisms for both microscale and nanoscale particles [27,28,83,85–88]. As mentioned previously, Du *et al.* [27] found that the dominant densification mechanism during the early stage of hot-press sintering of microscale ceramic particles is plastic deformation. That view is also shared by recent work of Xu *et al.* [83]. In contrast, our simulations indicate that plastic deformation is not the dominant sintering mechanism for nanoparticulate ceramics. For ceramic nanoparticles, several simulations of sintering with two and three nanoparticles have indicated as possible densification mechanisms surface diffusion, particle rotation and rearrangement, and grain boundary migration [42,45,85–89]. However, particle rotation and rearrangement are not observed in our results, because in our simulations the sintering process starts from the FCC arrangement of nanoparticles, which is the most compact packing. According to the results presented for AlN nanoparticles, strong surface diffusion is in fact observed for the AlN-8 and AlN-8-0.1 samples in the first 3 ns of sintering. The strong surface diffusion is mainly controlled by

the cation diffusion because Al has a much higher diffusivity than N as shown in Fig. 3. Similar behavior of Al cations was reported in the hot-press sintering of alumina [90]. As shown in Figs. 1(b) and 3, the fast surface diffusion of small nanoparticles significantly enhances the sintering densification, in agreement with previous simulation results. On the other hand, when the densification of the AlN-8 sample exceeds ∼98.7%, the diffusivity of the original surface atoms decreases. The densification process is then dominated by grain boundary migration and relaxation of the structure at grain boundaries and triple junctions. That is suggested by the increased diffusivity of second shell and core atoms. The presence of wrong bonds in the original core regions at 6 ns implied by the bond angle curves shown in Fig. 4(d) also indicates the occurrence of grain boundary migration. Our simulations for tens of nanoparticles provide a full description of the shift of the dominant densification mechanism during the hot-press sintering process of AlN nanoparticles from surface diffusion to grain boundary migration.

In the synthesis of dense nanocrystalline ceramics, it is very important to preserve the nanocrystalline characteristics. Therefore it is essential to prevent or minimize grain growth during the sintering of ceramic nanoparticles. To have a better understanding of the microstructure evolution, we evaluate the grain size evolution of all the initial nanoparticles in the AlN-8 and AlN-8-0.1 samples, as shown in Figs. 7(a) and 7(b). The results display a clear onset of the swift grain growth at ∼3 ns in the AlN-8 sample, yet the grain growth rate displayed by the AlN-8-0.1 sample is much lower, suggesting that ceramic nanoparticles sintered under higher pressures may have a larger average grain size than corresponding samples sintered at lower pressures. A similar pressure effect on grain growth during hot-press sintering was also reported in other studies [34,39].

However, studies have found that high pressure can inhibit the grain growth during the sintering process of titania if such high pressure can introduce phase transformation [26,91–93]. Arguably, the rationale is that nucleation of a new phase can potentially constrain grain boundary migration and prevent grain growth. For AlN, both simulation [49,94] and experimental results [95] indicate that a wurtzite-to-rocksalt phase transition occurs at a high pressure of ∼20 GPa. This value is reduced to ∼12 GPa at 1900 K [94]. According to the force balance argument, the pressure is usually intensified by a stress intensification factor ϕ in the grain boundary regions, due to the porosity [96]. Several derived ϕ expressions for different cases have indicated that it is sensitive to the density of the system, generally decreasing for increasing density [72,97–99]. For the case of a monosize spherical powder, the expression in Eq. (9) was proposed by Arzt *et al.* [96–98]:

$$\phi = \frac{1 - \rho_0}{\rho^2(\rho - \rho_0)}, \tag{9}$$

where ρ and ρ_0 are the current and initial densities, respectively. Thus it is possible to induce phase transition during the hot-press sintering process of AlN nanoparticles by applying a hydrostatic pressure lower than the critical value in order to suppress the grain growth. In fact, in this work, analysis indicates that 1 GPa pressure is sufficient to induce a wurtzite-to-rocksalt phase transformation at the grain boundary regions
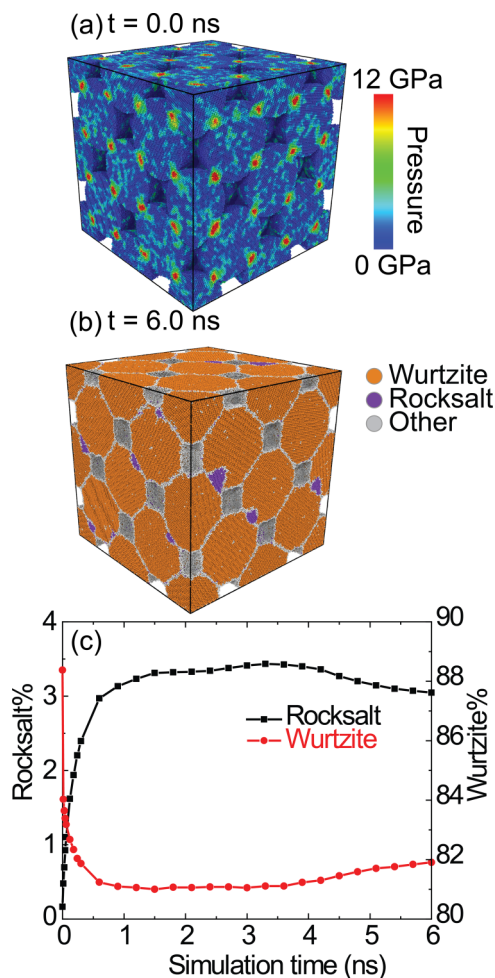
FIG. 10. Structural phase transition for the 16 nm sized nanoparticle system sintered under 1.0 GPa. (a) Local pressure distribution before sintering. (b) Crystalline structure after sintering for 6 ns. (c) Evolution of the volume fraction of rocksalt and wurtzite structures in the sintering system.

between nanoparticles in the AlN-16 sample. To evaluate the local stress distribution in the sample we calculate the Virial stress on each atom and average its value in a spherical voxel with radius of 7.35 Å [100]. As shown in Fig. 10(a), the local stress at grain boundaries at 0 ns exceeds 12 GPa, while the local stress in most of other regions is close to 0 GPa. The initial stress concentration leads to the formation of rocksalt AlN in the necking area as indicated in Fig. 10(b). We evaluate the evolution of the structural transformation by monitoring the volume fraction of AlN in the wurtzite and rocksalt structures. The results shown in Fig. 10(c) indicate that the structural transformation occurs swiftly in the first 0.5 ns of the sintering process and produce about 3% rocksalt in the sample, which is kept during the remaining sintering process. Since the swift grain growth does not occur in the AlN-16 sample, the suppression effect of the phase transition on the grain growth process cannot be evaluated here. For the other samples with smaller particle sizes, we do not observe this phase transformation even though they all have the same reduced density in the beginning. This is due to a much higher densification rate of samples AlN-12 and AlN-8

than sample AlN-16. For the case of small particles, the stress intensified at the grain boundary regions is released in a very short time (<0.5 ns), thus there is not enough time for the rocksalt nucleation process to occur in these samples. In contrast, in the sample AlN-16, the intensified stress at the grain boundary regions persists for a long time, triggering a local structural phase transformation for the rocksalt structure.

By tracking each grain in the AlN-8 sample, we observe a two-stage microstructural evolution during the hot-press sintering of AlN nanopowders, i.e., an initial grain size distribution broadening followed by a swift grain growth. Because the mobility of grain boundaries largely determines the grain growth rate, the swift grain growth occurs when grain boundaries are no more immobilized by the presence of pores as the number and the size of the pores decrease during the densification [32,33]. Thus, the key factor that defines the crossover between the two stages is the critical densification value. Fang *et al.* [32] reported that a general critical densification value for the sintering of nano-sized particles was ∼90%. A similar value was also found in the sintering of ∼60 nm Al_2O_3 nanoceramics [101] and ∼30 nm tungsten nanoparticles [102]. Our results in Fig. 7(c) show a similar trend for the relationship between grain size and reduced density, as reported by Fang *et al.* [32]. However, samples AlN-8 and AlN-8-0.1 display different critical densification values, 98.7% and 95%, respectively, suggesting that the densification threshold increases with the external pressure. Other samples with 12 and 16 nm sized nanoparticles also reach densifications higher than 90%. However, they do not display apparent microstructure coarsening, as shown in Fig. 2. These results suggest that small nanoparticles and high external pressure delay the onset of the swift grain growth to a higher densification value during the hot-press sintering process.

V. CONCLUSIONS

In summary, we performed MD simulations to investigate the densification process and microstructural evolution during the hot-press sintering of AlN nanoparticles. Three nanoparticle sizes of 8, 12, and 16 nm and two hydrostatic pressures of 0.1 and 1.0 GPa were used to clarify the effects of particle size and pressure on the sintering process. The AlN-8 sample displays a nearly full densification of ∼99%, yet also a significant microstructural coarsening, resulting in an average grain size of 11 nm. The results of the AlN-8 sample suggest a shift of densification mechanisms from surface diffusion to grain boundary migration and relaxation of the structure at grain boundaries and triple junctions as the sintering progresses. This shift is accompanied by a two-stage microstructural evolution. During the first stage, the sample experiences a fast densification, reaching a critical densification value, and a constrained microstructural evolution. In contrast, during the second stage, the sample undergoes intense microstructural coarsening while the densification slowly increases. In addition, results show a strong pressure effect on the densification as well as critical densification value of the AlN-8 sample, which increases densification and critical densification value from 96.2% to 99% and from 95% to 98.7%, respectively, when compared with the AlN-8-0.1 sample, i.e., when

hydrostatic pressure is increased from 0.1 to 1.0 GPa. The densification mechanisms as well as the rapid grain growth process we observed here are in excellent agreement with previous experimental investigations. This work highlights the atomistic mechanisms inherent to the fast densification of nanoceramics under hot-press sintering and is expected to support future work on the effects of temperature, pressure, and electric fields on the sintering process of nanoceramics

and in the search of effective methods to inhibit sintering grain growth.

[1] B. Feng, Y. Zhou, C. Peng, X. Li, J. Liu, Y. Wang, P. Rao, and J. Wu, Vibration assisted hot-press sintering of AlN ceramics, J. Am. Ceram. Soc. **98**, 1711 (2015).

[2] J. Zhan, Y. Wu, H. Zhang, J. Liu, J. Guo, C. Geng, S. Cui, and W. Tang, Secondary phases, microstructures and properties of AlN ceramics sintered by adding nitrate sintering additives, Adv. Appl. Ceram. **114**, 77 (2015).

[3] H. Zhao, W. Wang, Z. Fu, and H. Wang, Thermal conductivity and dielectric property of hot-pressing sintered AlN-BN ceramic composites, Ceram. Int. **35**, 105 (2009).

[4] K. M. Taylor and C. Lenie, Some properties of aluminum nitride, J. Electrochem. Soc. **107**, 308 (1960).

[5] R. Elfrink, T. M. Kamel, M. Goedbloed, S. Matova, D. Hohlfeld, Y. Van Andel, and R. Van Schaijk, Vibration energy harvesting with aluminum nitride-based piezoelectric devices, J. Micromech. Microengin. **19**, 8 (2009).

[6] W. Werdecker and F. Aldinger, Aluminum nitride-an alternative ceramic substrate for high power applications in microcircuits, IEEE Trans. Compon., Hybrids, Manuf. Technol. **7**, 399 (1984).

[7] R. T. Bondokov, S. G. Mueller, K. E. Morgan, G. A. Slack, S. Schujman, M. C. Wood, J. A. Smart, and L. J. Schowalter, Large-area AlN substrates for electronic applications: An industrial perspective, J. Cryst. Growth **310**, 4020 (2008).

[8] M. Fattahi, K. Vaferi, M. Vajdi, F. Sadegh Moghanlou, A. Sabahi Namini, and M. Shahedi Asl, Aluminum nitride as an alternative ceramic for fabrication of microchannel heat exchangers: A numerical study, Ceram. Int. **46**, 11647 (2020).

[9] C. Xiong, W. H. P. Pernice, X. Sun, C. Schuck, K. Y. Fong, and H. X. Tang, Aluminum nitride as a new material for chip-scale optomechanics and nonlinear optics, New J. Phys. **14**, 095014 (2012).

[10] C. Xiong, W. H. P. Pernice, and H. X. Tang, Low-loss, silicon integrated, aluminum nitride photonic circuits and their use for electro-optic signal processing, Nano Lett. **12**, 3562 (2012).

[11] M. L. Panchula and J. Y. Ying, Nanocrystalline aluminum nitride: II, sintering and properties, J. Am. Ceram. Soc. **86**, 1121 (2003).

[12] H. M. Lee, K. Bharathi, and D. K. Kim, Processing and characterization of aluminum nitride ceramics for high thermal conductivity, Adv. Eng. Mater. **16**, 655 (2014).

[13] Y. He and H. Wu, Investigation on low-temperature sintered aln nanoceramics with high thermal conductivity, Int. J. Appl. Ceram. Technol. **16**, 2101 (2019).

[14] H. S. Choi, H. N. Im, Y. M. Kim, A. Chavan, and S. J. Song, Structural, thermal and mechanical properties of aluminum nitride ceramics with CeO₂ as a sintering aid, Ceram. Int. **42**, 11519 (2016).

[15] J. Y. Qiu, Y. Hotta, K. Watari, K. Mitsuishi, and M. Yamazaki, Low-temperature sintering behavior of the nano-sized A1N powder achieved by super-fine grinding mill with Y₂O₃ and CaO additives, J. Eur. Ceram. Soc. **26**, 385 (2006).

[16] M. L. Panchula and J. Y. Ying, Synthesis and sintering of nanocrystalline alumina and aluminum nitride, Doctoral dissertation, Massachusetts Institute of Technology (1999).

[17] C. Greskovich and J. H. Rosolowski, Sintering of covalent solids, J. Am. Ceram. Soc. **59**, 336 (1976).

[18] S. M. Ognjanović and M. Winterer, Optimizing particle characteristics of nanocrystalline aluminum nitride, Powder Technol. **326**, 488 (2018).

[19] J. Pan, Solid-state diffusion under a large driving force and the sintering of nanosized particles, Philos. Mag. Lett. **84**, 303 (2004).

[20] Z. Z. Fang and H. Wang, Sintering of ultrafine and nanosized particles, in *Sintering of Advanced Materials* (Woodhead Publishing, 2010), pp. 434–473.

[21] J. R. Groza, Nanocrystalline powder consolidation methods, in *Nanostructured Materials* (William Andrew Publishing, 2007), pp. 173–233.

[22] Z. Yang, F. Gao, H. Du, L. Jin, L. Yan, Q. Hu, Y. Yu, S. Qu, X. Wei, Z. Xu, and Y.-J. Wang, Grain size engineered lead-free ceramics with both large energy storage density and ultrahigh mechanical properties, Nano Energy **58**, 768 (2019).

[23] S. F. Wang, J. Zhang, D. W. Luo, F. Gu, D. Y. Tang, Z. L. Dong, G. E. B. Tan, W. X. Que, T. S. Zhang, S. Li, and L. B. Kong, Transparent ceramics: Processing, materials and applications, Prog. Solid State Chem. **41**, 20 (2013).

[24] S. M. So, W. H. Choi, K. H. Kim, J. S. Park, M. S. Kim, J. Park, Y. S. Lim, and H. S. Kim, Mechanical properties of B4C–SiC composites fabricated by hot-press sintering, Ceram. Int. **46**, 9575 (2020).

[25] S.-C. Liao, Y.-J. Chen, B. H. Kear, and W. E. Mayo, High pressure/low temperature sintering of nanocrystalline alumina, Nanostruct. Mater. **10**, 1063 (1998).

[26] S. C. Liao, W. E. Mayo, and K. D. Pae, Theory of high pressure/low temperature sintering of bulk nanocrystalline TiO₂, Acta Mater. **45**, 4027 (1997).

[27] X. Du, Z. Zhang, Y. Wang, J. Wang, W. Wang, H. Wang, and Z. Fu, Hot-pressing kinetics and densification mechanisms of boron carbide, J. Am. Ceram. Soc. **98**, 1400 (2015).

[28] Y. Xiong, X. Du, M. Xiang, H. Wang, W. Wang, and Z. Fu, Densification mechanism during reactive hot pressing of B₄C-ZrO₂ mixtures, J. Eur. Ceram. Soc. **38**, 4167 (2018).

[29] M. Shahedi Asl and M. Ghassemi Kakroudi, Fractographical assessment of densification mechanisms in hot pressed ZrB₂-SiC composites, Ceram. Int. **40**, 15273 (2014).

[30] V. H. Nguyen, S. A. Delbari, M. Shahedi Asl, A. Sabahi Namini, M. Ghassemi Kakroudi, Y. Azizian-Kalandaragh, Q. Van Le, M. Mohammadi, and M. Shokouhimehr, Role of hot-pressing temperature on densification and microstructure of ZrB$_2$–SiC ultrahigh temperature ceramics, Int. J. Refract. Met. Hard Mater. **93**, 105355 (2020).

[31] W. Wang, Z. Fu, H. Wang, and R. Yuan, Influence of hot pressing sintering temperature and time on microstructure and mechanical properties of TiB$_2$ ceramics, J. Eur. Ceram. Soc. **22**, 1045 (2002).

[32] Z. Z. Fang and H. Wang, Densification and grain growth during sintering of nanosized particles, Int. Mater. Rev. **53**, 326 (2008).

[33] Z. Z. Fang, H. Wang, and V. Kumar, Coarsening, densification, and grain growth during sintering of nano-sized powders—a perspective, Int. J. Refract. Met. Hard Mater. **62**, 110 (2017).

[34] M. Zhang, Z. Zhou, T. Yuan, R. Li, W. Zhang, Y. Zhang, M. Wang, and S. Xie, Analysis of abnormal grain growth behavior during hot-press sintering of boron carbide, Ceram. Int. **46**, 16345 (2020).

[35] G. Riquet, S. Marinel, Y. Bréard, and C. Harnois, Sintering mechanism and grain growth in CaCu$_3$Ti$_4$O ceramics, Ceram. Int. **45**, 9185 (2019).

[36] B. Dargatz, J. Gonzalez-Julian, M. Bram, Y. Shinoda, F. Wakai, and O. Guillon, FAST/SPS sintering of nanocrystalline zinc oxide-part II: Abnormal grain growth, texture and grain anisotropy, J. Eur. Ceram. Soc. **36**, 1221 (2016).

[37] Z. Zhang, X. Duan, B. Qiu, L. Chen, P. Zhang, D. Cai, P. He, H. Zhang, Z. Wei, Z. Yang, D. Jia, and Y. Zhou, Microstructure evolution and grain growth mechanisms of H-BN ceramics during hot-pressing, J. Eur. Ceram. Soc. **40**, 2268 (2020).

[38] M. H. Lee, J. H. Park, S. D. Park, J. S. Rhyee, and M. W. Oh, Grain growth mechanism and thermoelectric properties of hot press and spark plasma sintered Na-doped PbTe, J. Alloys Compd. **786**, 515 (2019).

[39] X. Zhang, H. Gao, Z. Zhang, R. Wen, G. Wang, J. Mu, H. Che, and X. Zhang, Effects of pressure on densification behaviour, microstructures and mechanical properties of boron carbide ceramics fabricated by hot pressing, Ceram. Int. **43**, 6345 (2017).

[40] D. W. Brenner, in *Computer Modeling of Nanostructured Materials, Nanostructured Materials* (William Andrew Publishing, 2007), pp. 293–328.

[41] L. Sementa, G. Barcaro, S. Monti, and V. Carravetta, Molecular dynamics simulations of melting and sintering of si nanoparticles: A comparison of different force fields and computational models, Phys. Chem. Chem. Phys. **20**, 1707 (2018).

[42] P. Song and D. Wen, Molecular dynamics simulation of the sintering of metallic nanoparticles, J. Nanoparticle Res. **12**, 823 (2010).

[43] A. Chatterjee, R. K. Kalia, A. Nakano, A. Omeltchenko, K. Tsuruta, P. Vashishta, C.-K. Loong, M. Winterer, and S. Klein, Sintering, structure, and mechanical properties of nanophase SiC: A molecular-dynamics and neutron scattering study, Appl. Phys. Lett. **77**, 1132 (2000).

[44] M. Tavakol, M. Mahnama, and R. Naghdabadi, Shock wave sintering of Al/SiC metal matrix nano-composites: A molecular dynamics study, Comput. Mater. Sci. **125**, 255 (2016).

[45] V. N. Koparde and P. T. Cummings, Molecular dynamics simulation of titanium dioxide nanoparticle sintering, J. Phys. Chem. B **109**, 24280 (2005).

[46] B. Buesser, A. J. Gröhn, and S. E. Pratsinis, Sintering rate and mechanism of TiO$_2$ nanoparticles by molecular dynamics, J. Phys. Chem. C **115**, 11030 (2011).

[47] Y. Ren, Y. Zhang, Q. Mao, and H. Pitsch, Amorphous-to-crystalline transition during sintering of nascent TiO$_2$ nanoparticles in gas-phase synthesis: A molecular dynamics study, J. Phys. Chem. C **124**, 27763 (2020).

[48] P. S. Branicio, A. Nakano, R. K. Kalia, and P. Vashishta, Shock loading on AlN ceramics: A large scale molecular dynamics study, Int. J. Plast. **51**, 122 (2013).

[49] P. Vashishta, R. K. Kalia, A. Nakano, and J. P. Rino, Inter-action potential for aluminum nitride: A molecular dynamics study of mechanical and thermal properties of crystalline and amorphous aluminum nitride, J. Appl. Phys. **109**, 033514 (2011).

[50] H. Xiang, H. Li, and X. Peng, Comparison of different inter-atomic potentials for MD simulations of AlN, Comput. Mater. Sci. **140**, 113 (2017).

[51] H. Xiang, H. Li, T. Fu, Y. Zhao, C. Huang, G. Zhang, and X. Peng, Molecular dynamics simulation of AlN thin films under nanoindentation, Ceram. Int. **43**, 4068 (2017).

[52] P. Zhu and B. Li, Study on deformation behaviors of nanopillar textured AlN in nanoindentation using molecular dynamics, Ceram. Int. **47**, 4166 (2021).

[53] P. S. Branicio, R. K. Kalia, A. Nakano, and P. Vashishta, Shock-Induced Structural Phase Transition, Plasticity, and Brittle Cracks in Aluminum Nitride Geramic, Phys. Rev. Lett. **96**, 065502 (2006).

[54] Y. Zhao, X. Peng, T. Fu, C. Huang, H. Xiang, N. Hu, and C. Yan, Investigation of mechanical behaviour of amorphous aluminium nitride, Materialia **2**, 148 (2018).

[55] P. S. Branicio, R. K. Kalia, A. Nakano, P. Vashishta, F. Shimojo, and J. P. Rino, Atomistic damage mechanisms during hypervelocity projectile impact on AlN: A large-scale parallel molecular dynamics simulation study, J. Mech. Phys. Solids **56**, 1955 (2008).

[56] P. S. Branicio, J. Zhang, J. P. Rino, A. Nakano, R. K. Kalia, and P. Vashishta, Shock-induced microstructural response of mono- and nanocrystalline SiC ceramics, J. Appl. Phys. **123**, 145902 (2018).

[57] P. S. Branicio, J. Zhang, J. P. Rino, A. Nakano, R. K. Kalia, and P. Vashishta, Plane shock loading on mono- and nano-crystalline silicon carbide, Appl. Phys. Lett. **112**, 111909 (2018).

[58] P. S. Branicio and J. Zhang, Atomistic modeling of shock loading in SiC ceramics, in *Materials Research Society Symposium Proceedings* (MRS Online Proceedings Library (OPL), 2013), Vol. 1535, pp. 8–13.

[59] M. Mishra, C. Tangpatjaroen, and I. Szlufarska, Plasticity-controlled friction and wear in nanocrystalline SiC, J. Am. Ceram. Soc. **97**, 1194 (2014).

[60] I. Szlufarska, Atomistic simulations of nanoindentation, Mater. Today **9**, 42 (2006).

[61] I. Szlufarska, A crossover in the mechanical response of nanocrystalline ceramics, Science **309**, 911 (2005).

[62] C. Zhang, R. K. Kalia, A. Nakano, P. Vashishta, and P. S. Branicio, Deformation mechanisms and damage in α-alumina

under hypervelocity impact loading, J. Appl. Phys. **103**, 83508 (2008).

[63] C. Zhang, R. K. Kalia, A. Nakano, and P. Vashishta, Fracture initiation mechanisms in α -alumina under hypervelocity impact, Appl. Phys. Lett. **91**, 121911 (2007).

[64] A. Stukowski, Visualization and analysis of atomistic simulation data with OVITO–the open visualization tool, Model. Simul. Mater. Sci. Eng. **18**, 015012 (2010).

[65] P. M. Larsen, S. Schmidt, and J. Schiøtz, Robust structural identification via polyhedral template matching, Model. Simul. Mater. Sci. Eng. **24**, 055007 (2016).

[66] P. W. Hoffrogge, and L. A. Barrales-Mora, Grain-resolved kinetics and rotation during grain growth of nanocrystalline aluminium by molecular dynamics, Comput. Mater. Sci. **128**, 207 (2017).

[67] A. Stukowski, Computational analysis methods in atomistic modeling of crystals, JOM **66**, 399 (2014).

[68] See Supplemental Material at http://link.aps.org/supplemental/10.1103/PhysRevMaterials.5.096001 for porosity evolution, and animation for the microstructural evolution of each sample.

[69] K. Komeya and H. Inoue, Sintering of aluminium nitride: Particle size dependence of sintering kinetics, J. Mater. Sci. **4**, 1045 (1969).

[70] R. M. da Rocha, F. F. Sene, M. D. O. Juliani, and C. O. Davi, Effect of ZrB_2 particle size on pressureless sintering of ZrB_2-ß-Sic composites, J. Aerosp. Technol. Manag. **11**, e2819 (2019).

[71] B. C. Kim, J. H. Lee, J. J. Kim, and T. Ikegami, Rapid rate sintering of nanocrystalline indium tin oxide ceramics: Particle size effect, Mater. Lett. **52**, 114 (2002).

[72] R. L. Coble, Diffusion models for hot pressing with surface energy and pressure effects as driving forces, J. Appl. Phys. **41**, 4798 (1970).

[73] T. Sakai and M. Iwata, On the final stage in pressure sintering process, Jpn. J. Appl. Phys. **15**, 537 (1976).

[74] F. R. N. Nabarro, Deformation of crystals by the motion of single ions, in *Report of a Conference on the Strength of Solids* (The Physical Society, London, 1948) p. 75.

[75] C. Herring, Diffusional viscosity of a polycrystalline solid, J. Appl. Phys. **21**, 437 (2004).

[76] J. Li, X. Ren, Y. Zhang, and H. Hou, Silicon carbide low temperature sintering: The particle size effect of raw materials and sintering additive, Mater. Res. Express **7**, 035601 (2020).

[77] Y. Zou, Y. Wu, X. Guo, S. Tong, Z. Wang, and L. Zhang, Effect of particle size on the densification and dielectric properties of $BaTiO_3$ ceramics prepared by liquid phase sintering, Phys. Status Solidi **209**, 243 (2012).

[78] P. Barick, D. Chakravarty, B. P. Saha, R. Mitra, and S. V. Joshi, Effect of pressure and temperature on densification, microstructure and mechanical properties of spark plasma sintered silicon carbide processed with β-silicon carbide nanopowder and sintering additives, Ceram. Int. **42**, 3836 (2016).

[79] S. R. Bakshi, V. Musaramthota, D. Lahiri, V. Singh, S. Seal, and A. Agarwal, Spark plasma sintered tantalum carbide: Effect of pressure and nano-boron carbide addition on mi-

crostructure and mechanical properties, Mater. Sci. Eng. A **528**, 1287 (2011).

[80] S. Kobayashi, W. Kawai, and S. Wakayama, The effect of pressure during sintering on the strength and the fracture toughness of hydroxyapatite ceramics, J. Mater. Sci.: Mater. Med. **17**, 1089 (2006).

[81] A. Noviyanto, Effect of applied pressure during sintering on the densification and mechanical properties of SiCf/SiC composites prepared by electrophoretic infiltration, Makara J. Sci. **24**, 1 (2020).

[82] U. Anselmi-Tamburini, J. E. Garay, and Z. A. Munir, Fast low-temperature consolidation of bulk nanometric ceramic materials, Scr. Mater. **54**, 823 (2006).

[83] H. Xu, J. Zou, W. Wang, H. Wang, W. Ji, and Z. Fu, Densification mechanism and microstructure characteristics of nano- and micro-crystalline alumina by high-pressure and low temperature sintering, J. Eur. Ceram. Soc. **41**, 635 (2021).

[84] L. Malerba, D. Terentyev, P. Olsson, R. Chakarova, and J. Wallenius, Molecular dynamics simulation of displacement cascades in Fe-Cr alloys, J. Nucl. Mater. **329–333**, 1156 (2004).

[85] P. Zeng, S. Zajac, P. Clapp, and J. Rifkin, Nanoparticle sintering simulations, Mater. Sci. Eng. A **252**, 301 (1998).

[86] J. Jiang, P. Chen, and W. Sun, Monitoring micro-structural evolution during aluminum sintering and understanding the sintering mechanism of aluminum nanoparticles: A molecular dynamics study, J. Mater. Sci. Technol. **57**, 92 (2020).

[87] X. Wang and L. Benabou, Numerical modeling of low-temperature and low-pressure sintering of silver microparticles based on surface and grain boundary diffusion mechanisms, Mech. Adv. Mater. Struct. 1 (2020).

[88] J. M. Sestito, F. Abdeljawad, T. A. L. Harris, Y. Wang, and A. Roach, An atomistic simulation study of nanoscale sintering: The role of grain boundary misorientation, Comput. Mater. Sci. **165**, 180 (2019).

[89] J. S. Raut, R. B. Bhagat, and K. A. Fichthorn, Sintering of aluminum nanoparticles: A molecular dynamics study, Nanostruct. Mater. **10**, 837 (1998).

[90] R. C. Rossi and R. M. Fulrath, Final stage densification in vacuum hot-pressing of alumina, J. Am. Ceram. Soc. **48**, 558 (1965).

[91] S.-C. Liao, Y.-J. Chen, W. E. Mayo, and B. H. Kear, Transformation-assisted consolidation of bulk nanocrystalline TiO_2, Nanostruct. Mater. **11**, 553 (1999).

[92] B. H. Kear, J. Colaizzi, W. E. Mayo, and S. C. Liao, On the processing of nanocrystalline and nanocomposite ceramics, Scr. Mater. **44**, 2065 (2001).

[93] M. Mazaheri, Z. Razavi Hesabi, and S. K. Sadrnezhaad, Two-step sintering of titania nanoceramics assisted by anatase-to-rutile phase transformation, Scr. Mater. **59**, 139 (2008).

[94] A. Siegel, K. Parlinski, and U. D. Wdowik, *Ab initio* calculation of structural phase transitions in AlN crystal, Phys. Rev. B **74**, 104116 (2006).

[95] T. Mashimo, M. Uchino, A. Nakamura, T. Kobayashi, E. Takasawa, T. Sekine, Y. Noguchi, H. Hikosaka, K. Fukuoka, and Y. Syono, Yield properties, phase transition, and equation of state of aluminum nitride (AlN) under shock compression up to 150 GPa, J. Appl. Phys. **86**, 6710 (1999).

[96] M. N. Rahaman, Kinetics and mechanisms of densification, in *Sintering of Advanced Materials* (Elsevier, 2010), pp. 33–64.

[97] E. Arzt, M. F. Ashby, and K. E. Easterling, Practical applications of hotisostatic pressing diagrams: Four case studies, Metall. Trans. A **14**, 211 (1983).

[98] A. S. Helle, K. E. Easterling, and M. F. Ashby, Hot-isostatic pressing diagrams: New developments, Acta Metall. **33**, 2163 (1985).

[99] J. M. Vieira and R. J. Brook, Kinetics of hot-pressing: The semilogarithmic law, J. Am. Ceram. Soc. **67**, 245 (1984).

[100] P. S. Branicio and D. J. Srolovitz, Local stress calculation in simulations of multicomponent systems, J. Comput. Phys. **228**, 8467 (2009).

[101] J. Li and Y. Ye, Densification and grain growth of Al_2O_3 nanoceramics during pressureless sintering, J. Am. Ceram. Soc. **89**, 139 (2006).

[102] H. Wang, Z. Zak Fang, and K. S. Hwang, Kinetics of initial coarsening during sintering of nanosized powders, in *Metallurgical and Materials Transactions A: Physical Metallurgy and Materials Science* (Springer, 2011), Vol. 42, pp. 3534–3542.